Available online at www.sciencedirect.com
ScienceDirect
Journal of Sound and Vibration 306 (2007) 618–635
JOURNAL OF SOUND AND VIBRATION
www.elsevier.com/locate/jsvi

An Eulerian coordinate-based method for analysing the structural vibrations of a solid of revolution rotating about its main axis

J. Fayos, L. Baeza*, F.D. Denia, J.E. Tarancón

Departamento de Ingeniería Mecánica y de Materiales, Universidad Politécnica de Valencia, Camino de Vera s.n., 46022 Valencia, Spain

Received 30 January 2007; received in revised form 29 May 2007; accepted 31 May 2007
Available online 27 July 2007

Abstract

This article presents a technique for modelling the dynamic response of spinning solids of revolution. The method is especially adequate for considering those cases where the interesting displacements and the external forces are associated with points at which the Eulerian coordinates are constant. The method is based on the modal properties of solids of revolution: any deformed shape of the solid after rotation can be calculated as a linear combination of the non-rotating modes. The obtained formulation takes account of the flexibility of the solid and the inertial and gyroscopic effects due to the rotation. In this paper, the method is applied to a cylinder (considering an analytical and a numerical approach), and to a railway wheelset.

1. Introduction

A model for obtaining the dynamic response of a flexible solid of revolution has numerous practical utilities such as rotor shafts [1–3], power generators and motors [4,5], vehicles [6] and certain manufacturing processes [7]. During the development of the dynamic model of some of these applications we focus our attention on the external surface shape of the solid, rather than the position of each material point. The importance of this approach lies in the fact that the enveloping surface of the deformed solid of revolution determines the interaction with the other non-rotating structures in the system. For example, the dynamic models of railway vehicles consider the wheel–rail contact point and the positions of the wheelset axle boxes; these points are set on a theoretical non-rotating surface that envelopes the solid.

Since the interest is on a non-rotating surface, it is easy to find works where the coupled dynamics between two orthogonal planes containing the solid axis is neglected. The dynamic coupling is due to the inertial effects associated with the rotation and in some cases, it is not negligible even if the angular velocity is low. There is a lack of knowledge on how this coupling occurs. A first approach to consider the rotating effects was made by different researchers through a beam model. Sheu and Yang [8] developed a rotating Rayleigh beam model

*Corresponding author. Tel.: +34 963877621; fax: +34 963877629.
E-mail address: lbaeza@mcm.upv.es (L. Baeza).

0022-460X/$ - see front matter © 2007 Elsevier Ltd. All rights reserved.
doi:10.1016/j.jsv.2007.05.051

which allows to obtain the modal shapes and natural frequencies of the system. They stated that there is no angular velocity above which the system is unstable; however there is a finite set of critical angular velocities. In the Ref. [9] the dynamic coupling between two non-rotating orthogonal planes containing the undeformed beam was concluded. The trajectory of any of the centre beam points was deduced to be a hypotrochoid curve. The dynamic response was obtained as a function of a single parameter computed from the angular velocity and the beam slenderness ratio. Non-negligible coupling between orthogonal planes containing the axis is possible mainly if the slenderness ratio of the beam is small. A general procedure for obtaining the dynamic response of rotating solids was deduced by Brown and Shabana [10]. The basis was the methodology for elastic bodies presented in Ref. [11]. The deduced formulation is general and can be applied to any solid geometry. They adopted a set of Lagrangian coordinates based on a modal approach. The method was applied to an Euler beam in their paper.

The present work develops a model for obtaining the dynamic response of a general elastic solid of revolution that turns around its main axis. The model is based on the method presented in the Ref. [10]. In order to facilitate the study of the interaction with non-rotating structures, the model of Brown and Shabana [10] was modified through the adoption of Eulerian coordinates. This set of coordinates avoids recalculating the formulation in each time step during the integration if the external forces are applied in a constant spatial point and if the displacements in a constant spatial point are required. The proposed coordinate set and its properties are discussed in Section 2 of this article. The complete method is presented in Sections 3 (formulae) and 4 (computational method). The paper shows some results in Section 5, where the model is applied to a cylinder and a railway wheelset.

2. Kinematic model of the elastic solid of revolution

The methodology employed to model the kinematics of the solid is a general approach in Continuum Mechanics of the type proposed by Mase and Mase [12]. For each time instant t, we define a Reference Configuration (henceforth, RC) that corresponds to the position of each particle in the undeformed solid. We adopt an inertial Cartesian frame $Ox_1x_2x_3$, where x_1 is the main axis of the solid of revolution in its RC. The only large displacement corresponds to the spinning velocity of the solid, that is $\mathbf{\Omega} = \Omega\vec{x}$. We assume the hypothesis of small displacements for the remaining motions.

Let $\mathbf{u} = (u_1, u_2, u_3)^{\mathrm{T}}$ be the position vector of a particle in the RC at the initial instant $t = 0$. The position of the particle in the RC at the time instant t, is calculated through the expression $\mathbf{Au}$, where

$$\mathbf{A} = \begin{pmatrix} 1 & 0 & 0 \\ 0 & \cos\theta & -\sin\theta \\ 0 & \sin\theta & \cos\theta \end{pmatrix} \tag{1}$$

is the rotation matrix corresponding to the angular displacement θ. Let $\mathbf{\Phi(u)}$ be a mass-normalised matrix field of mode shapes of the solid. To this end, we consider a finite number N of vibration modes of the solid. The mode shapes are calculated for the free solid at the initial time instant $t = 0$. They include the deformed mode shapes of the solid and the rigid body modes. The position of a particle can be expressed as follows:

$$\mathbf{r}(\mathbf{u}, t) = \mathbf{A}(\mathbf{u} + \mathbf{\Phi(u)p}), \tag{2}$$

where $\mathbf{p} = \mathbf{p}(t)$ is the vector of modal coordinates. This approach is shown in Fig. 1.

The mode shapes functions $\mathbf{\Phi}$ for general solids are function of time if they are expressed through the non-rotating system $Ox_1x_2x_3$. This condition is not required if the solid has symmetry of revolution. Taking into account that any deformed shape of the solid is obtained through a linear combination of the mode shapes, the spatial coordinates associated with the solid can be calculated as follows:

$$\mathbf{s}(\mathbf{v}, t) = \mathbf{v} + \mathbf{\Phi(v)q}, \tag{3}$$

where $\mathbf{q} = \mathbf{q}(t)$ is a set of coordinates, and $\mathbf{v}$ is the Eulerian coordinate associated with the undeformed geometry. This second approach is shown in Fig. 2.

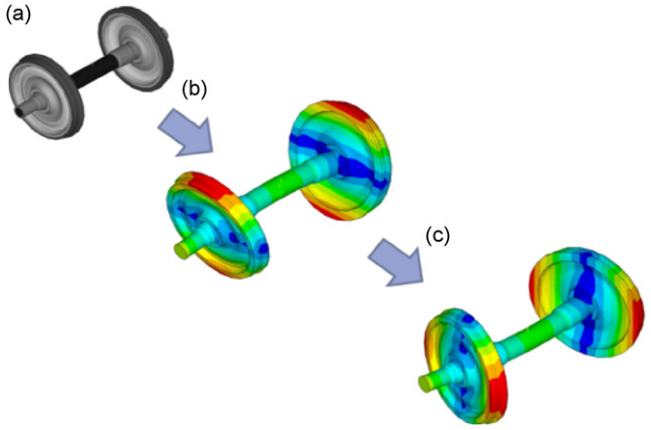

Fig. 1. Lagrangian approach: (a) reference configuration at initial time instant given by $\mathbf{u}$. (b) Deformed shape after rotation given by $\mathbf{u}+\mathbf{\Phi}(\mathbf{u})\mathbf{p}$. (c) Final shape given by $\mathbf{A}(\mathbf{u}+\mathbf{\Phi}(\mathbf{u})\mathbf{p})$.

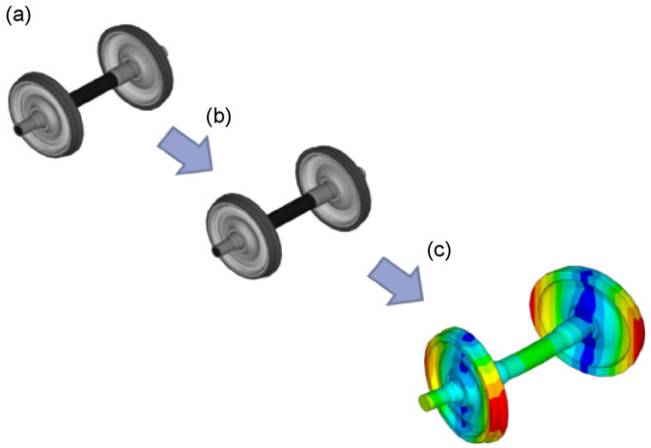

Fig. 2. Eulerian approach: (a) reference configuration at initial instant given by $\mathbf{u}$; (b) reference configuration at instant t given by $\mathbf{v}$; and (c) final shape given by $\mathbf{v}+\mathbf{\Phi}(\mathbf{v})\mathbf{q}$.

If at a certain time instant the particle defined through the Lagrangian coordinate $\mathbf{r}$ is situated in the spatial point $\mathbf{s}$, then the following relationships are obtained:

$$\mathbf{A}(\mathbf{u}+\mathbf{\Phi}(\mathbf{u})\mathbf{p}) = \mathbf{v}+\mathbf{\Phi}(\mathbf{v})\mathbf{q}, \tag{4}$$

$$\mathbf{A}\mathbf{u} = \mathbf{v} \tag{5}$$

and operating

$$\mathbf{A}\mathbf{\Phi}(\mathbf{A}^{\mathrm{T}}\mathbf{v})\mathbf{p} = \mathbf{\Phi}(\mathbf{v})\mathbf{q}. \tag{6}$$

Defining the matrix $\mathbf{B} = \mathbf{B}(t)$ as

$$\mathbf{q} = \mathbf{B}\mathbf{p}, \tag{7}$$

the relationship (7) can be introduced in Eq. (6), resulting in

$$\mathbf{A}\mathbf{\Phi}(\mathbf{A}^{\mathrm{T}}\mathbf{v}) = \mathbf{\Phi}(\mathbf{v})\mathbf{B}. \tag{8}$$

Matrix $\mathbf{B}$ is deduced by multiplying Eq. (8) by $\rho\mathbf{\Phi}(\mathbf{v})^{\mathrm{T}}$ and then integrating over the volume, ρ being the density. Due to the orthogonal properties of the modes, matrix $\mathbf{B}$ yields

$$\mathbf{B} = \int_{\mathrm{RCV}} \rho\mathbf{\Phi}(\mathbf{v})^{\mathrm{T}}\mathbf{A}\mathbf{\Phi}(\mathbf{A}^{\mathrm{T}}\mathbf{v})\,\mathrm{d}\upsilon, \tag{9}$$

where the integral is extended to the RC volume (RCV). Matrix $\mathbf{B}$ is an orthogonal matrix, i.e.

$$\mathbf{B}^{\mathrm{T}}\mathbf{B} = \mathbf{I}_N, \tag{10}$$

where $\mathbf{I}_N$ is the $N \times N$ identity matrix.

3. Equation of motion

The kinetic energy of the system is calculated as

$$T = \frac{1}{2}\int_{\mathrm{SV}} \rho \dot{\mathbf{r}}^{\mathrm{T}}\dot{\mathbf{r}}\,\mathrm{d}\upsilon \tag{11}$$

in which the integral is extended to the volume of the solid (SV). The integral limits will be changed from the SV to RCV if we express the integrand through $\mathbf{u}$ or $\mathbf{v}$. The elastic energy can be computed by means of the following expression:

$$V = \frac{1}{2}\left(\mathbf{p}^{\mathrm{T}}\,\tilde{\mathbf{K}}\,\mathbf{p}\right), \tag{12}$$

where $\tilde{\mathbf{K}}$ being a diagonal matrix containing the square of the undamped natural frequencies associated with the modes $\mathbf{\Phi}$. The equation of motion can be obtained through the Lagrange's equations. From Eqs. (11) and (12) it can be deduced that

$$\int_{\mathrm{SV}} \rho\left[\frac{\partial \dot{\mathbf{r}}^{\mathrm{T}}}{\partial \dot{\mathbf{p}}}\ddot{\mathbf{r}} + \left(\frac{\mathrm{d}}{\mathrm{d}t}\frac{\partial \dot{\mathbf{r}}^{\mathrm{T}}}{\partial \dot{\mathbf{p}}} - \frac{\partial \dot{\mathbf{r}}^{\mathrm{T}}}{\partial \mathbf{p}}\right)\dot{\mathbf{r}}\right]\mathrm{d}\upsilon + \tilde{\mathbf{K}}\,\mathbf{p} = \mathbf{Q}_{\mathbf{p}}. \tag{13}$$

The generalised force $\mathbf{Q}_{\mathbf{p}}$ is calculated from the generic volume forces $\mathbf{f}$ as follows:

$$\mathbf{Q}_{\mathbf{p}}(t) = \int_{\mathrm{RCV}} \frac{\partial \mathbf{r}(u)^{\mathrm{T}}}{\partial \mathbf{p}}\mathbf{f}(\mathbf{u},t)\,\mathrm{d}\upsilon = \int_{\mathrm{RCV}} \mathbf{\Phi}(\mathbf{u})^{\mathrm{T}}\mathbf{A}^{\mathrm{T}}\mathbf{f}(\mathbf{u},t)\,\mathrm{d}\upsilon. \tag{14}$$

It should be stated that net forces are particular cases of the volume forces. The development of Eq. (13) provides the next equation of motion (which can be found in Appendix A of this article)

$$\ddot{\mathbf{p}} + 2\Omega\tilde{\mathbf{J}}\,\dot{\mathbf{p}} + (\tilde{\mathbf{K}} - \Omega^2\,\tilde{\mathbf{E}})\mathbf{p} = \mathbf{Q}_{\mathbf{p}} + \Omega^2\mathbf{L}, \tag{15}$$

where the matrices in Eq. (15) are

$$\mathbf{J} = \mathbf{A}^{\mathrm{T}}\mathbf{A}_{\theta}, \quad \tilde{\mathbf{J}} = \int_{\mathrm{RCV}} \rho\mathbf{\Phi}^{\mathrm{T}}\mathbf{J}\mathbf{\Phi}\,\mathrm{d}\upsilon, \tag{16}$$

$$\mathbf{E} = -\mathbf{A}_{\theta\theta}\mathbf{A}^{\mathrm{T}}, \quad \tilde{\mathbf{E}} = \int_{\mathrm{RCV}} \rho\mathbf{\Phi}^{\mathrm{T}}\mathbf{E}\mathbf{\Phi}\,\mathrm{d}\upsilon, \tag{17}$$

$$\mathbf{L} = \int_{\mathrm{RCV}} \rho\mathbf{\Phi}(\mathbf{u})^{\mathrm{T}}\mathbf{E}\mathbf{u}\,\mathrm{d}\upsilon, \tag{18}$$

$\mathbf{A}_{\theta}$ and $\mathbf{A}_{\theta\theta}$ being the first and second derivative of the matrix $\mathbf{A}$ which is defined in Eq. (1) with respect to the angle θ. Vector $\mathbf{L}$ contains constant radial centrifugal forces that produce axis-symmetrical radial displacements. Consequently the non-zero terms of the vector $\mathbf{L}$ are associated with axis-symmetrical radial modes such as breathing and umbrella modes.

The equation of motion adapted for an Eulerian approach is obtained by substituting Eq. (7) into Eq. (15), i.e.

$$\ddot{\mathbf{q}} + (2\Omega\mathbf{B}\,\tilde{\mathbf{J}}\,\mathbf{B}^{\mathrm{T}} + 2\mathbf{B}\dot{\mathbf{B}}^{\mathrm{T}})\dot{\mathbf{q}} + (\mathbf{B}\,\tilde{\mathbf{K}}\,\mathbf{B}^{\mathrm{T}} - \Omega^2\mathbf{B}\,\tilde{\mathbf{E}}\,\mathbf{B}^{\mathrm{T}} + 2\Omega\mathbf{B}\,\tilde{\mathbf{J}}\,\dot{\mathbf{B}}^{\mathrm{T}} + \mathbf{B}\ddot{\mathbf{B}}^{\mathrm{T}})\mathbf{q} = \mathbf{B}\mathbf{Q}_{\mathbf{p}} + \Omega^2\mathbf{B}\mathbf{L}, \tag{19}$$

where the following relations are satisfied (see Appendix C for details):

$$\mathbf{B}\tilde{\mathbf{J}}\mathbf{B}^{\mathrm{T}} = \tilde{\mathbf{J}}, \tag{20}$$

$$\mathbf{B}\tilde{\mathbf{K}}\mathbf{B}^{\mathrm{T}} = \tilde{\mathbf{K}}, \tag{21}$$

$$\mathbf{B}\tilde{\mathbf{E}}\mathbf{B}^{\mathrm{T}} = \tilde{\mathbf{E}}, \tag{22}$$

$$\mathbf{B}\tilde{\mathbf{J}}\dot{\mathbf{B}}^{\mathrm{T}} = \Omega\tilde{\mathbf{J}}\mathbf{Z}^{\mathrm{T}}, \tag{23}$$

$$\mathbf{BL} = \mathbf{L}. \tag{24}$$

The matrix $\mathbf{Z}$ is defined as

$$\mathbf{Z} = \frac{1}{\Omega}\dot{\mathbf{B}}\mathbf{B}^{\mathrm{T}}. \tag{25}$$

The Appendix B shows that

$$\mathbf{Z} = \tilde{\mathbf{J}} + \tilde{\mathbf{G}}, \tag{26}$$

where

$$\tilde{\mathbf{G}} = \int_{\mathrm{RCV}} \rho\left(\sum_{i=1}^{3}\frac{\partial\boldsymbol{\Phi}^{\mathrm{T}}}{\partial v_i}(\mathbf{Jv})_i\right)\boldsymbol{\Phi}\,\mathrm{d}\upsilon. \tag{27}$$

If the external forces are always applied in the same spatial points, we can reformulate the generalised force term. The spatial and the temporal variables in the force vector can be separated as follows:

$$\mathbf{f}(\mathbf{v},t) = \mathbf{F}(\mathbf{v})\mathbf{g}(t). \tag{28}$$

Replacing Eq. (28) in the generalised force vector in Eq. (19), it yields

$$\mathbf{BQ}_{\mathrm{p}}(t) = \mathbf{B}\int_{\mathrm{RCV}}\boldsymbol{\Phi}(\mathbf{u})^{\mathrm{T}}\mathbf{A}^{\mathrm{T}}\mathbf{f}(\mathbf{Au},t)\,\mathrm{d}\upsilon = \int_{\mathrm{RCV}}\boldsymbol{\Phi}(\mathbf{v})^{\mathrm{T}}\mathbf{f}(\mathbf{v},t)\,\mathrm{d}\upsilon = \int_{\mathrm{RCV}}\boldsymbol{\Phi}(\mathbf{v})^{\mathrm{T}}\mathbf{F}(\mathbf{v})\,\mathrm{d}\upsilon\mathbf{g}(t). \tag{29}$$

The previous integral does not depend on time. We define $\tilde{\mathbf{F}}$ as

$$\tilde{\mathbf{F}} = \int_{\mathrm{RCV}}\boldsymbol{\Phi}(\mathbf{v})^{\mathrm{T}}\mathbf{F}(\mathbf{v})\,\mathrm{d}\upsilon. \tag{30}$$

By substituting Eqs. (20)–(27) and (30) into Eq. (19), we have

$$\ddot{\mathbf{q}} + 2\Omega\tilde{\mathbf{G}}^{\mathrm{T}}\dot{\mathbf{q}} + \left(\tilde{\mathbf{K}} + \Omega^2\left(\tilde{\mathbf{J}}\tilde{\mathbf{J}}^{\mathrm{T}} - \tilde{\mathbf{G}}\tilde{\mathbf{G}}^{\mathrm{T}} - \tilde{\mathbf{E}}\right)\right)\mathbf{q} = \tilde{\mathbf{F}}\,\mathbf{g}(t) + \Omega^2\mathbf{L}. \tag{31}$$

The latter equation can be compacted in the final form

$$\ddot{\mathbf{q}} + 2\Omega\tilde{\mathbf{G}}^{\mathrm{T}}\dot{\mathbf{q}} + \left(\tilde{\mathbf{K}} + \Omega^2\tilde{\mathbf{C}}\right)\mathbf{q} = \tilde{\mathbf{F}}\,\mathbf{g}(t) + \Omega^2\mathbf{L}, \tag{32}$$

where $\tilde{\mathbf{C}} = \tilde{\mathbf{J}}\tilde{\mathbf{J}}^{\mathrm{T}} - \tilde{\mathbf{G}}\tilde{\mathbf{G}}^{\mathrm{T}} - \tilde{\mathbf{E}}$. One advantage of this formulation is that $\tilde{\mathbf{G}}$, $\tilde{\mathbf{K}}$, $\tilde{\mathbf{C}}$, $\tilde{\mathbf{F}}$ and $\mathbf{L}$ do not depend on time and consequently, they can be calculated at the beginning of the simulation.

4. Computational method

The method developed previously can be formulated analytically only in simple cases, such as a beam model. In order to analyse more complex structures such as railway wheelsets or non-uniform section shafts, the present section proposes a numerical methodology. Taking into account that modal analysis of general structures is usually calculated through a finite element (FE) model, we adopted the FE method in order to obtain the matrices associated with the equation of motion (32).

The FE modal analysis provides the modal solution in the nodes of the solid mesh. Let $\mathbf{\Phi}_{\mathrm{FE}}$ be the modal matrix obtained from the FE model. The modal function in the eth element can be estimated as follows:

$$\mathbf{\Phi}_e(\mathbf{v}) = \mathbf{N}_e(\mathbf{v})\mathbf{\Phi}_{\mathrm{FE}}, \tag{33}$$

where $\mathbf{N}_e(\mathbf{v})$ is the FE basis function of the element e. If we substitute the last expression into Eqs. (16)–(18), (27) and (30), we obtain

$$\tilde{\mathbf{J}} = \mathbf{\Phi}_{\mathrm{FE}}^{\mathrm{T}}\left(\sum_{e=1}^{N_E}\int_{\mathrm{RCV}_e}\rho\mathbf{N}_e(\mathbf{v})^{\mathrm{T}}\mathbf{J}\mathbf{N}_e(\mathbf{v})\,\mathrm{d}\upsilon\right)\mathbf{\Phi}_{\mathrm{FE}}, \tag{34}$$

$$\tilde{\mathbf{G}} = \mathbf{\Phi}_{\mathrm{FE}}^{\mathrm{T}}\left(\sum_{e=1}^{N_E}\int_{\mathrm{RCV}_e}\rho\left(\sum_{i=1}^{3}\frac{\partial\mathbf{N}_e(\mathbf{v})^T}{\partial v_i}(\mathbf{J}\mathbf{v})_i\right)\mathbf{N}_e(\mathbf{v})\,\mathrm{d}\upsilon\right)\mathbf{\Phi}_{\mathrm{FE}}, \tag{35}$$

$$\tilde{\mathbf{E}} = \mathbf{\Phi}_{\mathrm{FE}}^{\mathrm{T}}\left(\sum_{e=1}^{N_E}\int_{\mathrm{RCV}_e}\rho\mathbf{N}_e(\mathbf{v})^{\mathrm{T}}\mathbf{E}\mathbf{N}_e(\mathbf{v})\,\mathrm{d}\upsilon\right)\mathbf{\Phi}_{\mathrm{FE}}, \tag{36}$$

$$\tilde{\mathbf{F}} = \mathbf{\Phi}_{\mathrm{FE}}^{\mathrm{T}}\left(\sum_{e=1}^{N_E}\int_{\mathrm{RCV}_e}\mathbf{N}_e(\mathbf{v})^{\mathrm{T}}\mathbf{F}(\mathbf{v})\,\mathrm{d}\upsilon\right), \tag{37}$$

$$\mathbf{L} = \mathbf{\Phi}_{\mathrm{FE}}^{\mathrm{T}}\left(\sum_{e=1}^{N_E}\int_{\mathrm{RCV}_e}\rho\mathbf{N}_e(\mathbf{v})^{\mathrm{T}}\mathbf{E}\mathbf{v}\,\mathrm{d}\upsilon\right), \tag{38}$$

where N_E is the number of elements in the mesh and the RCV_e is the volume of the eth element. These formulae are used in Eq. (32) to obtain all the terms required. The computational method was implemented in the open source programme FEAP [13].

5. Case studies

The present section provides examples where the developed formulation has been applied. The method can be considered in different ways, depending on how we obtain the modal properties associated with the solid of revolution. In order to compare the results of two approaches, we first study a spinning cylinder with simply supported ends where the modal properties are calculated analytically through a Rayleigh beam model and numerically through a solid FE model. The former case allowed the validation of the proposed method since this problem was also analysed in Ref. [8]. Two radii are considered: $R_1 = 100\,\mathrm{mm}$ and $R_2 = 50\,\mathrm{mm}$. The beam properties can be found in Table 1 and the first six natural frequencies are presented in Table 2. The slenderer beam lets the comparison of the Rayleigh beam model with the FE model results. This geometry, however, gives rise to a weak dynamic coupling between two orthogonal planes containing the beam axis. The coupling

Table 1
Properties of the beam model

Length	$L = 1500\,\mathrm{mm}$
Density	$\rho = 7800\,\mathrm{kg/m^3}$
Section radii	$R_1 = 100\,\mathrm{mm}$, $R_2 = 50\,\mathrm{mm}$
Young's modulus	$E = 2.1 \times 10^{11}\,\mathrm{N/m^2}$
Poisson's ratio	$\nu = 0.3$

Table 2
Natural frequencies of the cylinders (in Hz)

Mode index	Mode type	Radius 50 mm		Radius 100 mm	
		MEF	Rayleigh beam model	MEF	Rayleigh beam model
1	1st Bending mode	89.03	90.43	176.88	180.14
2	2nd Bending mode	351.40	361.75	669.41	720.54
3	3rd Bending mode	774.14	813.93	1394.19	1621.22
4	4th Bending mode	1339.06	1446.99	2270.70	2882.18
5	1st Torsion mode	1060.55	—	1060.53	—
6	1st Breathing mode	1729.46	—	1727.69	—

is more important for the cylinder with greater radius. Nevertheless, the behaviour of the greater radius cylinder is influenced by the shear deformation and consequently the Rayleigh model does not fit the results obtained through FEM.

Secondly, a more complex model is considered consisting of a railway wheelset. The associated equation of motion shows not only a non-negligible coupling between the vertical and the horizontal planes, but also the coupling appears between different modal frequencies.

5.1. Cylinder with simply supported ends modelled as a Rayleigh beam

The beam properties are the radius R, the length L, the Young's modulus E, the density ρ, the section area A and the inertia I. From Ref. [14], the nth mass-normalised mode shape calculated in the neutral fibre of the beam is

$$\phi_n(x_1) = \frac{1}{\sqrt{m_n}} \sin\left(\frac{n\pi x_1}{L}\right) \tag{39}$$

and the nth natural frequency is

$$\omega_n = \sqrt{\frac{EI(n\pi)^4}{2L^3 m_n}}, \tag{40}$$

where m_n has the following expression:

$$m_n = \frac{1}{2}\rho AL\left(1 - (n\pi)^2 \frac{I}{AL^2}\right). \tag{41}$$

If N modes of the beam are considered, matrix $\mathbf{\Phi}$ is given by

$$\mathbf{\Phi} = \begin{bmatrix} -x_2\dfrac{\mathrm{d}\phi_1}{\mathrm{d}x_1} & -x_3\dfrac{\mathrm{d}\phi_1}{\mathrm{d}x_1} & \cdots & -x_2\dfrac{\mathrm{d}\phi_N}{\mathrm{d}x_1} & -x_3\dfrac{\mathrm{d}\phi_N}{\mathrm{d}x_1} \\ \phi_1 & 0 & \cdots & \phi_N & 0 \\ 0 & \phi_1 & \cdots & 0 & \phi_N \end{bmatrix}. \tag{42}$$

The adimensional parameter g_n (for $n = 1,\ldots,$) is introduced as

$$g_n = \frac{\rho I(n\pi)^2}{2Lm_n}. \tag{43}$$

The matrices $\tilde{\mathbf{G}}$ and $\tilde{\mathbf{C}}$ are in this case

$$\tilde{\mathbf{G}} = \left[\begin{array}{cc:cc:c:cc} 0 & g_1 & 0 & 0 & \cdots & 0 & 0 \\ -g_1 & 0 & 0 & 0 & \cdots & 0 & 0 \\ \hdashline 0 & 0 & 0 & g_2 & \cdots & 0 & 0 \\ 0 & 0 & -g_2 & 0 & \cdots & 0 & 0 \\ \hdashline \vdots & \vdots & \vdots & \vdots & \ddots & \vdots & \vdots \\ \hdashline 0 & 0 & 0 & 0 & \cdots & 0 & g_N \\ 0 & 0 & 0 & 0 & \cdots & -g_N & 0 \end{array}\right], \tag{44}$$

$$\tilde{\mathbf{C}} = \left[\begin{array}{cc:cc:c:cc} -g_1 & 0 & 0 & 0 & \cdots & 0 & 0 \\ 0 & -g_1 & 0 & 0 & \cdots & 0 & 0 \\ \hdashline 0 & 0 & -g_2 & 0 & \cdots & 0 & 0 \\ 0 & 0 & 0 & -g_2 & \cdots & 0 & 0 \\ \hdashline \vdots & \vdots & \vdots & \vdots & \ddots & \vdots & \vdots \\ \hdashline 0 & 0 & 0 & 0 & \cdots & -g_N & 0 \\ 0 & 0 & 0 & 0 & \cdots & 0 & -g_N \end{array}\right]. \tag{45}$$

Other boundary conditions for the Rayleigh beam model provide similar $\tilde{\mathbf{G}}$ and $\tilde{\mathbf{C}}$ matrices where the non-zero entries are in the same position than the precedent case. However the numerical values have been found to be the same for both matrices (the g_n parameter) only if the beam has simply supported ends.

The first four g_n values for the $R_1 = 100\,\text{mm}$ radius cylinder are the following:

$$g_1 = 1.08473 \times 10^{-2}, \quad g_2 = 4.20216 \times 10^{-2}, \quad g_3 = 8.98302 \times 10^{-2}, \quad g_4 = 1.49269 \times 10^{-1}. \tag{46}$$

The same parameters for the $R_2 = 50\,\text{mm}$ radius cylinder are

$$g_1 = 2.73406 \times 10^{-3}, \quad g_2 = 1.08473 \times 10^{-2}, \quad g_3 = 2.40799 \times 10^{-2}, \quad g_4 = 4.20216 \times 10^{-2}. \tag{47}$$

5.2. *Cylinder with simply supported ends modelled through a solid FE approach*

Fig. 3 shows one of the meshes considered for the FE simulation. The FE model implements solid elements (mainly eight-noded hexahedron elements). The modal coordinates are chosen by following the indices defined

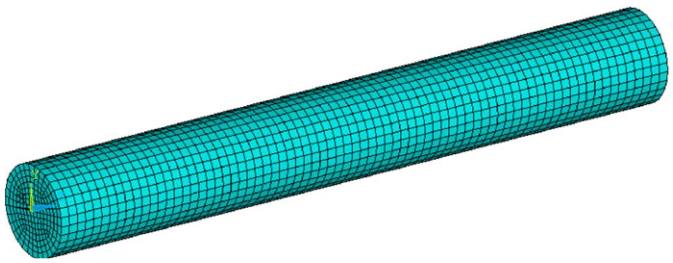

Fig. 3. FE mesh of the cylinder.

in Table 2. By applying Eqs. (34)–(37), the matrices $\tilde{\mathbf{G}}$ and $\tilde{\mathbf{C}}$ are

$$\tilde{\mathbf{G}} = \left[\begin{array}{cc:cc:cc:cc:cc} 0 & \tilde{G}_1 & 0 & 0 & 0 & 0 & 0 & 0 & 0 & 0 \\ -\tilde{G}_1 & 0 & 0 & 0 & 0 & 0 & 0 & 0 & 0 & 0 \\ \hdashline 0 & 0 & 0 & \tilde{G}_2 & 0 & 0 & 0 & 0 & 0 & 0 \\ 0 & 0 & -\tilde{G}_2 & 0 & 0 & 0 & 0 & 0 & 0 & 0 \\ \hdashline 0 & 0 & 0 & 0 & 0 & \tilde{G}_3 & 0 & 0 & 0 & 0 \\ 0 & 0 & 0 & 0 & -\tilde{G}_3 & 0 & 0 & 0 & 0 & 0 \\ \hdashline 0 & 0 & 0 & 0 & 0 & 0 & 0 & \tilde{G}_4 & 0 & 0 \\ 0 & 0 & 0 & 0 & 0 & 0 & -\tilde{G}_4 & 0 & 0 & 0 \\ \hdashline 0 & 0 & 0 & 0 & 0 & 0 & 0 & 0 & 0 & -\tilde{G}_{5,6} \\ \hdashline 0 & 0 & 0 & 0 & 0 & 0 & 0 & 0 & \tilde{G}_{5,6} & 0 \end{array}\right], \tag{48}$$

$$\tilde{\mathbf{C}} = \operatorname{diag}\left(-\tilde{C}_1 \quad -\tilde{C}_1 \,\vdots\, -\tilde{C}_2 \quad -\tilde{C}_2 \,\vdots\, -\tilde{C}_3 \quad -\tilde{C}_3 \,\vdots\, -\tilde{C}_4 \quad -\tilde{C}_5 \,\vdots\, -\tilde{C}_5 \,\vdots\, -\tilde{C}_6 \right). \tag{49}$$

The coefficients in Eqs. (48) and (49) for the $R_1 = 100\,\text{mm}$ radius cylinder are

$$\begin{aligned} &\tilde{G}_1 = 1.01418 \times 10^{-2}, \quad \tilde{G}_2 = 3.34913 \times 10^{-2}, \quad \tilde{G}_3 = 5.78728 \times 10^{-2}, \\ &\tilde{G}_4 = 7.64661 \times 10^{-2}, \quad \tilde{G}_{5,6} = 4.72596 \times 10^{-2}, \end{aligned} \tag{50}$$

$$\begin{aligned} &\tilde{C}_1 = 1.01984 \times 10^{-2}, \quad \tilde{C}_2 = 3.40008 \times 10^{-2}, \quad \tilde{C}_3 = 5.96499 \times 10^{-2}, \\ &\tilde{C}_4 = 7.98716 \times 10^{-2}, \quad \tilde{C}_5 = 9.82364 \times 10^{-1}, \quad \tilde{C}_6 = 2.28426 \times 10^{-3}. \end{aligned} \tag{51}$$

The coefficients for the $R_2 = 50\,\text{mm}$ radius cylinder are

$$\begin{aligned} &\tilde{G}_1 = 2.62673 \times 10^{-3}, \quad \tilde{G}_2 = 9.99684 \times 10^{-3}, \quad \tilde{G}_3 = 2.07960 \times 10^{-2}, \\ &\tilde{G}_4 = 3.33952 \times 10^{-2}, \quad \tilde{G}_{5,6} = 2.28727 \times 10^{-2}, \end{aligned} \tag{52}$$

$$\begin{aligned} &\tilde{C}_1 = 2.62588 \times 10^{-3}, \quad \tilde{C}_2 = 1.00175 \times 10^{-2}, \quad \tilde{C}_3 = 2.09189 \times 10^{-2}, \\ &\tilde{C}_4 = 3.38040 \times 10^{-2}, \quad \tilde{C}_5 = 9.73875 \times 10^{-1}, \quad \tilde{C}_6 = 5.44035 \times 10^{-4}. \end{aligned} \tag{53}$$

5.3. Comparison between analytical and numerical model of the cylinder

The results in Sections 5.1 and 5.2 provide qualitative information about the influence of the model and the coupling between two orthogonal planes containing the cylinder axis. The Rayleigh beam model is more suitable if the cylinder is slender and consequently the matrices calculated by means of numerical and analytical models are more similar for the 50 mm radius cylinder. The matrix $\tilde{\mathbf{G}}$ couples the modes of multiplicity 2. The entries in the matrices $\tilde{\mathbf{G}}$ and $\tilde{\mathbf{C}}$ are numerically bigger for the plump cylinder and therefore the effect of the angular velocity may be more noticeable as was deduced in Ref. [9].

More quantitative information can be obtained from Figs. 4 and 5. Fig. 4 shows the direct FRF (receptance) calculated for a point at a distance of 1050 mm from the cylinder end. The receptances were calculated for the

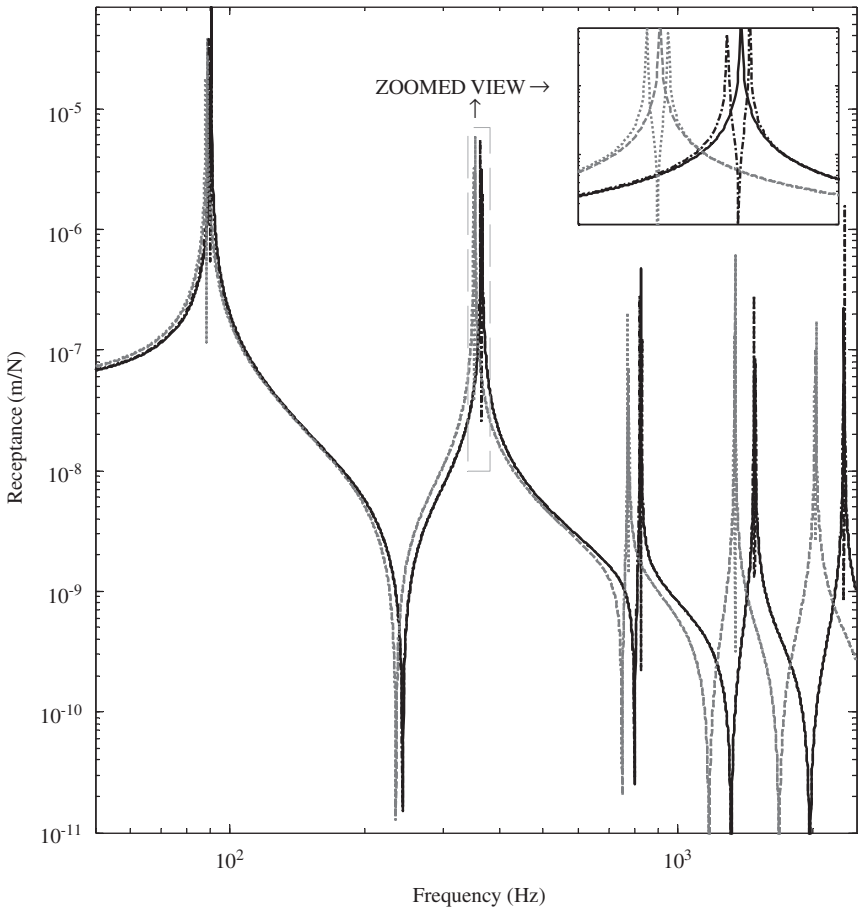

Fig. 4. Direct receptance function for a biarticulated cylinder with $R_2 = 50$ mm. Analytical model and $\Omega = 0$ in black continuous trace; analytical model and $\Omega = 10\,000$ rev/min in black dash-dot trace; FEM and $\Omega = 0$ in grey dash trace; FEM and $\Omega = 10\,000$ rev/min in grey dot trace.

cylinder with $R_2 = 50$ mm radius through the analytical and numerical models. The results were performed for a non-rotating cylinder and a spinning cylinder at 10000 rev/min. It can be observed that each peak in the non-rotating FRF doubles into two peaks in the rotating FRF.

The previous result makes difficult to analyse the model influence through the matrices $\tilde{\mathbf{G}}$ and $\tilde{\mathbf{C}}$ because the natural frequencies included in the matrix $\tilde{\mathbf{K}}$ depend on the model type. In order to discard the influence of matrix $\tilde{\mathbf{K}}$, the comparison of the FEM and Rayleigh beam FRF was carried out in Fig. 5, but implementing the same $\tilde{\mathbf{K}}$ matrix in both models. The calculation was done for different angular velocities of the cylinder with $R_1 = 100$ mm. It can be observed that the differences between the models due to the matrices $\tilde{\mathbf{G}}$ and $\tilde{\mathbf{C}}$ are only significant if the angular velocity of the cylinder is very high.

5.4. Railway wheelset with free boundary conditions through a FE approach

The FE mesh is shown in Fig. 6. The model has 5232 solid elements. The total length of the wheelset is 2261 mm, the wheel diameter is 1016 mm and the mechanical properties of the material are those from Table 1. The first 14 modes are described in Table 3 and those which involve elastic deformation are represented in Fig. 7.

The numerical values of the matrices $\tilde{\mathbf{G}}$, $\tilde{\mathbf{C}}$, $\tilde{\mathbf{K}}$ and $\mathbf{L}$ for 14 modal coordinates are shown in Eqs. (54)–(57). Fig. 8 outlines the matrices $\tilde{\mathbf{G}}$ and $\tilde{\mathbf{C}}$ for 50 modal coordinates. The matrix $\tilde{\mathbf{G}}$ couples the modes of multiplicity 2 at the same frequency, but the coupling also exists between modes at

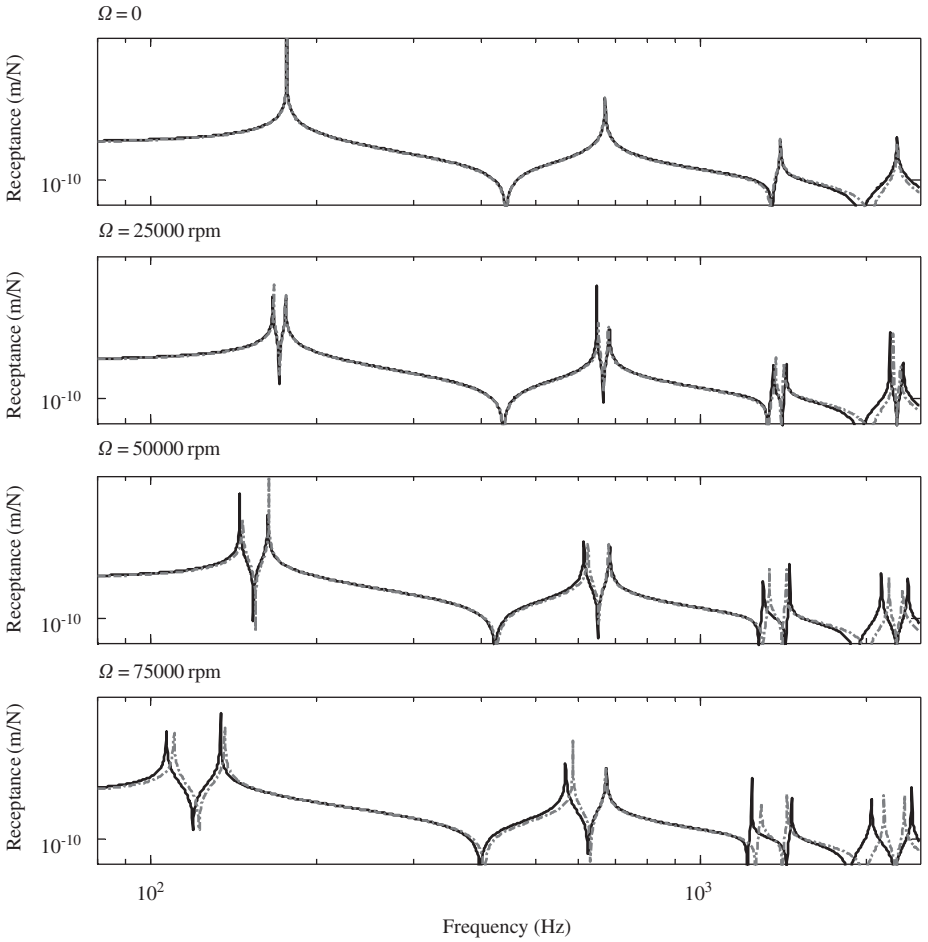

Fig. 5. Direct receptance function for a cylinder with $R_1 = 100$ mm calculated for 0, 25 000, 50 000 and 75 000 rev/min through the analytical (black continuous trace) and FE (grey dash-dot trace) approach. The natural frequencies are forced to be identical by imposing the same matrix $\tilde{\mathbf{K}}$.

different frequencies

$$\tilde{\mathbf{G}} = \left[\begin{array}{cccccc|cccccccc}
0 & 0 & 0 & 0 & 0 & 0 & 0 & 0 & 0 & 0 & 0 & 0 & 0 & 0 \\
 & 0 & 0 & 0 & 0 & 0 & 0 & 0 & 0 & 0 & 0 & 0 & 0 & 0 \\
 & & 0 & 0 & 0 & 0 & 0 & 0 & 0 & 0 & 0 & 0 & 0 & 0 \\
 & & & 0 & -0.10125 & 0 & 0 & 0 & 0 & 0.289694 & 0 & 0 & 0 & 0 \\
 & & & & 0 & 0 & 0 & 0 & 0 & 0 & -0.28969 & 0 & 0 & 0 \\
 & & & & & 0 & 0 & 0 & 0 & 0 & 0 & -1.352×10^{-2} & 0 & 0 \\
\hline
 & & & & & & 0 & 0 & 0 & 0 & 0 & 0 & 0 & 0 \\
 & & & & & & & 0 & -0.79624 & 0 & 0 & 0 & 0 & 0.36156 \\
 & & & & \text{ANTISYM} & & & & 0 & 0 & 0 & 0 & -0.36156 & 0 \\
 & & & & & & & & & 0 & 0.86717 & 0 & 0 & 0 \\
 & & & & & & & & & & 0 & 0 & 0 & 0 \\
 & & & & & & & & & & & 0 & 0 & 0 \\
 & & & & & & & & & & & & 0 & -0.25754 \\
 & & & & & & & & & & & & & 0
\end{array}\right], \tag{54}$$

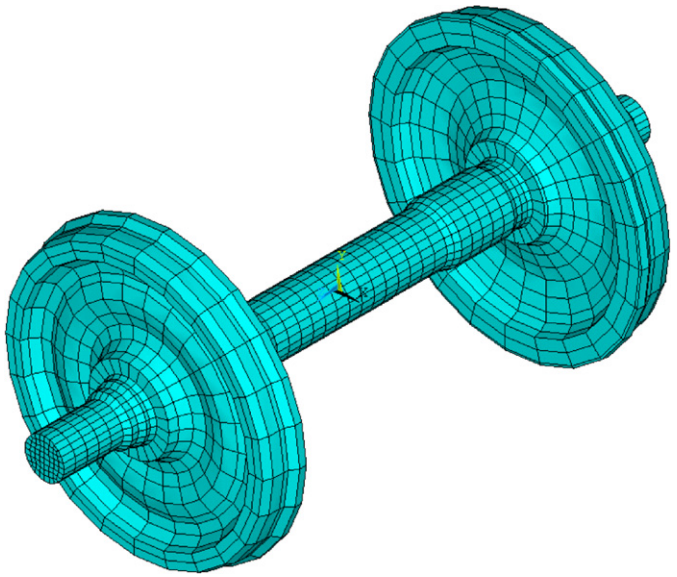

Fig. 6. FE mesh of a railway wheelset.

Table 3
Vibration modes of a railway wheelset

Mode number	Frequency (Hz)	Type
1–6	0	Rigid body
7	80.0	1st Torsion mode
8	93.7	1st Bending mode, horizontal plane
9	93.7	1st Bending mode, vertical plane
10	146.8	2nd Bending mode, horizontal plane
11	146.8	2nd Bending mode, vertical plane
12	226.7	1st Umbrella mode
13	287.6	3rd Bending mode, horizontal plane
14	287.6	3rd Bending mode, vertical plane

$$\tilde{\mathbf{C}} = \left[\begin{array}{cccccc:cccccccc}
0 & 0 & 0 & 0 & 0 & 0 & 0 & 0 & 0 & 0 & 0 & 0 & 0 & 0 \\
 & 0 & 0 & 0 & 0 & 0 & 0 & 0 & 0 & 0 & 0 & 0 & 0 & 0 \\
 & & 0 & 0 & 0 & 0 & 0 & 0 & 0 & 0 & 0 & 0 & 0 & 0 \\
 & & & -0.10125 & 0 & 0 & 0 & 0 & 0 & 0 & 0.28969 & 0 & 0 & 0 \\
 & & & & -0.10125 & 0 & 0 & 0 & 0 & 0.28969 & 0 & 0 & 0 & 0 \\
 & & & & & -0.99999 & 0 & 0 & 0 & 0 & 0 & 0 & 0 & 0 \\
\hdashline
 & & & & & & -1 & 0 & 0 & 0 & 0 & 0 & 0 & 0 \\
 & & & & & & & -0.79635 & 0 & 0 & 0 & 0 & 0.36205 & 0 \\
 & & & & & & & & -0.79634 & 0 & 0 & 0 & 0 & 0.36205 \\
 & & & \text{SYM} & & & & & & -0.86787 & 0 & 0 & 0 & 0 \\
 & & & & & & & & & & -0.86787 & 0 & 0 & 0 \\
 & & & & & & & & & & & -4.7746 \times 10^{-3} & 0 & 0 \\
 & & & & & & & & & & & & -0.26027 & 0 \\
 & & & & & & & & & & & & & -0.26027
\end{array}\right], \quad (55)$$

$$\tilde{\mathbf{K}} = diag[0 \;\; 0 \;\; 0 \;\; 0 \;\; 0 \;\; 0 \;\vdots\; 252876.7 \;\; 346748.8 \;\; 346748.8 \;\; 851233.1 \;\; 851233.1 \;\; 202815.1 \;\; 3266316.7 \;\; 3266316.7], \quad (56)$$

$$\mathbf{L} = \left[0 \;\; 0 \;\; 0 \;\; 0 \;\; 0 \;\; 0 \;\vdots\; 0 \;\; 0 \;\; 0 \;\; 0 \;\; 0 \;\; 0.16252984 \;\; 0 \;\; 0\right]^{\mathrm{T}}. \quad (57)$$

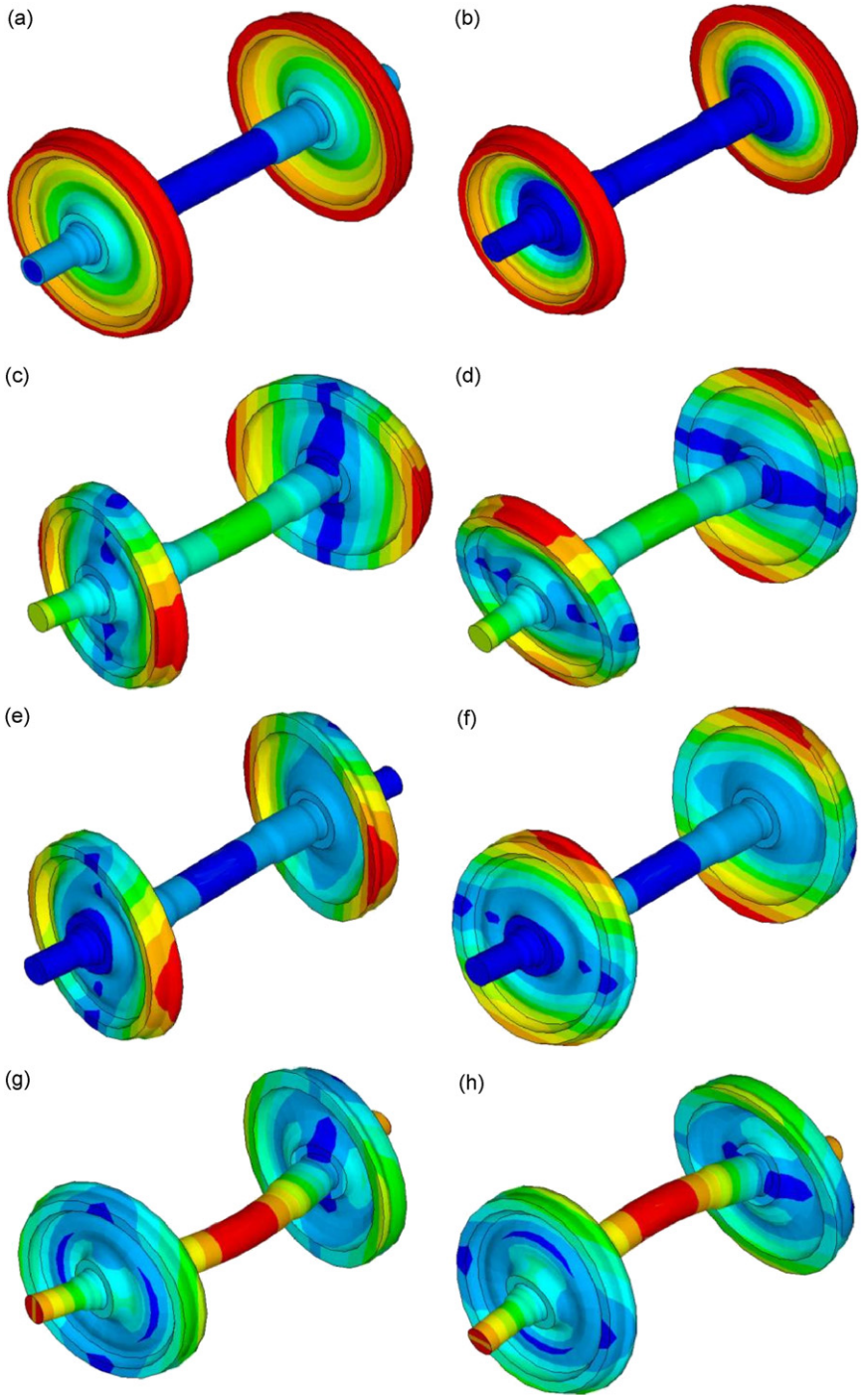

Fig. 7. Elastic modes of the wheelset: (a) Mode 7, (b) Mode 12, (c) Mode 8, (d) Mode 9, (e) Mode 10, (f) Mode 11, (g) Mode 13, and (h) Mode 14.

5.5. *Receptance function of the railway wheelset*

Fig. 9 shows the direct receptance function of the wheelset calculated for the vertical displacements of the contact point. The calculation was performed for three angular velocities: 0, 500 rev/min (95.8 km/h) and 1000 rev/min. The spectrum is shown in the range of the 1st and 2nd flexural modes (multiplicity 2) and the

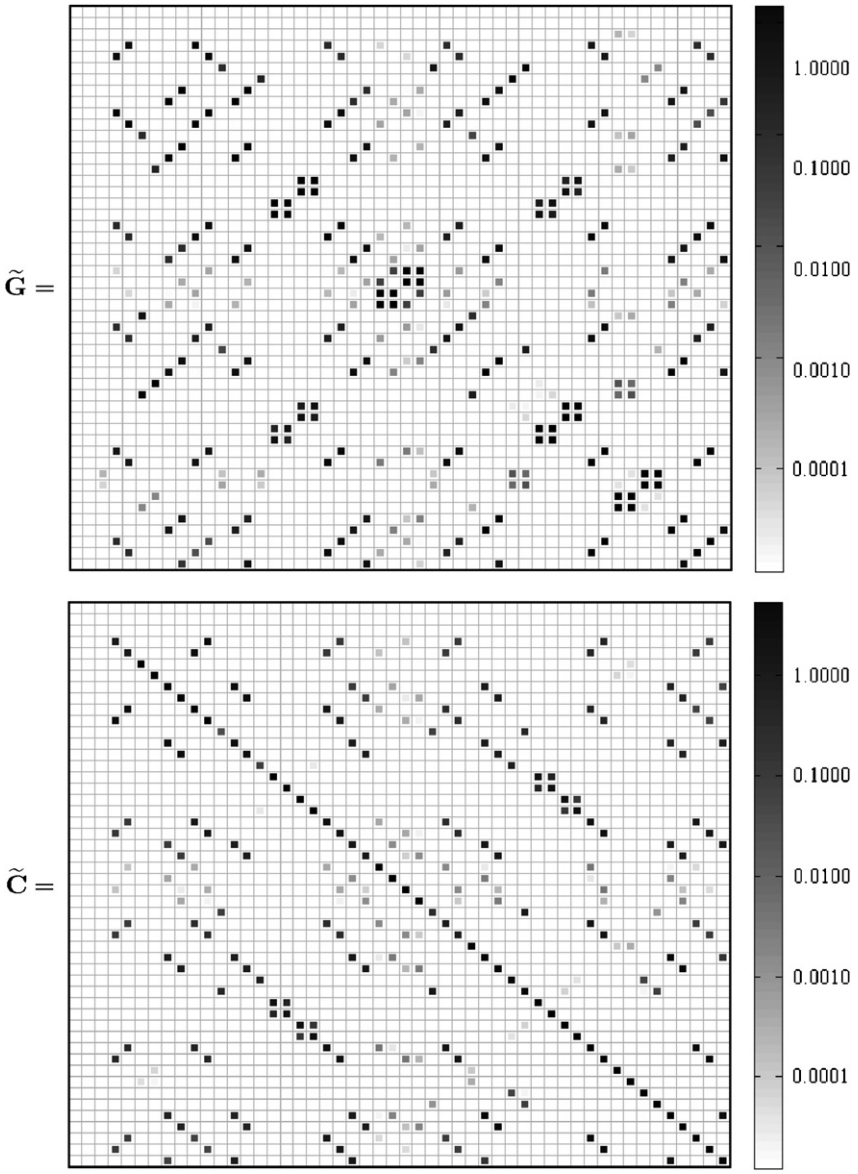

Fig. 8. Map of the matrices $\tilde{\mathbf{G}}$ and $\tilde{\mathbf{C}}$ for 50 modal coordinates.

umbrella mode (multiplicity 1). It can be observed that each resonance peak associated with a mode with multiplicity 2 of the non-rotating wheelset gives rise to two peaks when the angular velocity is non-zero. However, the resonances associated with the modes with multiplicity 1 do not depend on the angular velocity of the wheelset.

6. Conclusions

This article develops a complete method for modelling the dynamics of an elastic solid of revolution that rotates about its main axis. This model is designed for those cases where the interest lies in the enveloping surface of the solid, rather than the study of each material point. This viewpoint is especially useful for complex systems formed by rotating and non-rotating solids, where the displacements and velocities of the

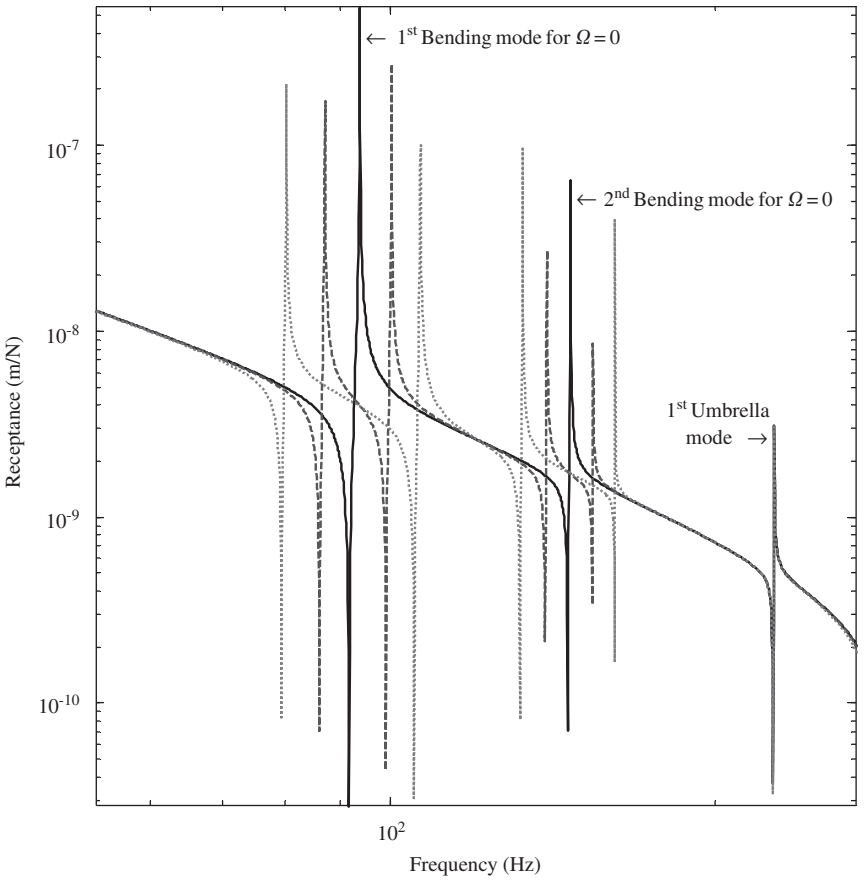

Fig. 9. Receptance function for the contact point for a railway wheelset. $\Omega = 0$ in black continuous trace. $\Omega = 500$ rev/min (aprox. 100 km/h) in dark grey dash trace. $\Omega = 1000$ rev/min in grey dot trace.

non-rotating substructures and the displacements and velocities of the enveloping surface of the spinning solid of revolution establish the coupling forces between the substructures.

The method is based on a modal approach where the mechanical properties of the solids are introduced through the modal properties of the non-rotating structure. The final formulation consists of a set of linear ODEs where their components do not depend on time. Consequently, the matrices are calculated once in the beginning of the simulation and the computational costs are considerably reduced.

The proposed technique is applied to several cases: (1) two cylinders with different radii where the modal properties are obtained by means of a Rayleigh beam model and through a FE model; and (2) a railway wheelset. The comparison of the results between the FEM and the Rayleigh model for the cylinders reveals small discrepancies due to the different approaches under consideration. The differences are smaller in the slenderer cylinder, as expected.

Regarding the coupling between two orthogonal planes containing the solid axis, it depends on the off-diagonal terms of the matrices $\tilde{\mathbf{G}}$ and $\tilde{\mathbf{C}}$. An analysis of these matrices for the Rayleigh beam model shows that the coupling exists between modes at the same frequency, while non-coincident frequency modes are uncoupled. The coupling is stronger if the slenderness of the beam is small. Nevertheless, more complex systems like a wheelset provide models where the coupling is not negligible and appears even between modes of different frequencies.

As a result of the gyroscopic effects, each peak in the FRF associated with a mode with multiplicity 2 gives rise to two resonances, one at lower frequency and the other at higher frequency. The frequency of the former peak in the FRF converges to zero with the angular velocity of the solid. Nevertheless the peaks associated with the modes with multiplicity 1 are not influenced by the angular velocity of the solid.

Acknowledgement

This research has been financed by the Projects T79/2006 (Ministerio de Fomento - Metro de Madrid - CDM) and TRA2007-67167 (Ministerio de Educación y Ciencia - FEDER).

Appendix A

The calculation of the terms involved in Eq. (13) yields

$$\dot{\mathbf{r}} = \Omega \mathbf{A}_\theta(\mathbf{u} + \mathbf{\Phi p}) + \mathbf{A\Phi}\dot{\mathbf{p}}, \tag{A.1}$$

$$\ddot{\mathbf{r}} = \Omega^2 \mathbf{A}_{\theta\theta}(\mathbf{u} + \mathbf{\Phi p}) + 2\Omega \mathbf{A}_\theta \mathbf{\Phi}\dot{\mathbf{p}} + \mathbf{A\Phi}\ddot{\mathbf{p}}, \tag{A.2}$$

$$\frac{\partial \dot{\mathbf{r}}^{\mathrm{T}}}{\partial \dot{\mathbf{p}}} \ddot{\mathbf{r}} = \mathbf{\Phi}^{\mathrm{T}} \mathbf{A}^{\mathrm{T}} \left(\Omega^2 \mathbf{A}_{\theta\theta}(\mathbf{u} + \mathbf{\Phi p}) + 2\Omega \mathbf{A}_\theta \mathbf{\Phi}\dot{\mathbf{p}} + \mathbf{A\Phi}\ddot{\mathbf{p}} \right), \tag{A.3}$$

$$\frac{\mathrm{d}}{\mathrm{d}t} \frac{\partial \dot{\mathbf{r}}^{\mathrm{T}}}{\partial \dot{\mathbf{p}}} = \frac{\partial \dot{\mathbf{r}}^{\mathrm{T}}}{\partial \mathbf{p}} = \Omega \mathbf{\Phi}^{\mathrm{T}} \mathbf{A}_\theta^{\mathrm{T}} \Rightarrow \left(\frac{\mathrm{d}}{\mathrm{d}t} \frac{\partial \dot{\mathbf{r}}^{\mathrm{T}}}{\partial \dot{\mathbf{p}}} - \frac{\partial \dot{\mathbf{r}}^{\mathrm{T}}}{\partial \mathbf{p}} \right) \dot{\mathbf{r}} = 0. \tag{A.4}$$

where $\mathbf{A}_\theta$ and $\mathbf{A}_{\theta\theta}$ are the first and second derivative of the matrix $\mathbf{A}$ defined in Eq. (1) with respect the angle θ. Replacing Eqs. (A.1)–(A.4) into Eq. (13) leads to

$$\ddot{\mathbf{p}} + 2\Omega \int_{\mathrm{RCV}} \rho \mathbf{\Phi}^{\mathrm{T}} \mathbf{J} \mathbf{\Phi} \, \mathrm{d}\upsilon \, \dot{\mathbf{p}} + \left(\tilde{\mathbf{K}} - \Omega^2 \int_{\mathrm{RCV}} \rho \mathbf{\Phi}^{\mathrm{T}} \mathbf{E} \mathbf{\Phi} \, \mathrm{d}\upsilon \right) \mathbf{p} = \mathbf{Q}_{\mathbf{p}} + \Omega^2 \int_{\mathrm{RCV}} \rho \mathbf{\Phi}^{\mathrm{T}} \mathbf{E} \mathbf{u} \, \mathrm{d}\upsilon. \tag{A.5}$$

It can be easily proved that $\mathbf{J}$ and $\mathbf{E}$ are given by

$$\mathbf{E} = \begin{pmatrix} 0 & 0 & 0 \\ 0 & 1 & 0 \\ 0 & 0 & 1 \end{pmatrix}, \quad \mathbf{J} = \begin{pmatrix} 0 & 0 & 0 \\ 0 & 0 & -1 \\ 0 & 1 & 0 \end{pmatrix}. \tag{A.6}$$

From Eqs. (8) and (17)

$$\begin{aligned} B \int_{\mathrm{RCV}} \rho \mathbf{\Phi}(\mathbf{u})^{\mathrm{T}} \mathbf{E} \mathbf{u} \, \mathrm{d}\upsilon &= - \int_{\mathrm{RCV}} \rho \mathbf{B} \mathbf{\Phi}(\mathbf{u})^{\mathrm{T}} \mathbf{A}^{\mathrm{T}} \mathbf{A}_{\theta\theta} \mathbf{u} \, \mathrm{d}\upsilon = - \int_{\mathrm{RCV}} \rho \mathbf{\Phi}(\mathbf{Au})^{\mathrm{T}} \mathbf{A} \mathbf{A}^{\mathrm{T}} \mathbf{A}_{\theta\theta} \mathbf{u} \, \mathrm{d}\upsilon \\ &= - \int_{\mathrm{RCV}} \rho \mathbf{\Phi}(\mathbf{Au})^{\mathrm{T}} \mathbf{A}_{\theta\theta} \mathbf{u} \, \mathrm{d}\upsilon = - \int_{\mathrm{RCV}} \rho \mathbf{\Phi}(\mathbf{Au})^{\mathrm{T}} \mathbf{A}_{\theta\theta} \mathbf{A}^{\mathrm{T}} \mathbf{Au} \, \mathrm{d}\upsilon = \int_{\mathrm{RCV}} \rho \mathbf{\Phi}(\mathbf{Au})^{\mathrm{T}} \mathbf{E} \mathbf{Au} \, \mathrm{d}\upsilon \\ &= \int_{\mathrm{RCV}} \rho \mathbf{\Phi}(\mathbf{v})^{\mathrm{T}} \mathbf{E} \mathbf{v} \, \mathrm{d}\upsilon. \end{aligned} \tag{A.7}$$

Eq. (15) is obtained from Eq. (A.5) by defining the matrices given in Eqs. (16) and (17).

Appendix B

Considering the orthogonal properties of matrix $\mathbf{B}$, the combination of Eqs. (5) and (8) yields

$$\mathbf{A}^{\mathrm{T}} \mathbf{\Phi}(\mathbf{Au}) = \mathbf{\Phi}(\mathbf{u}) \mathbf{B}^{\mathrm{T}}. \tag{B.1}$$

The matrix $\mathbf{\Phi}(\mathbf{u})$ does not depend on time. However $\mathbf{\Phi}(\mathbf{Au})$ is a function of time through the matrix $\mathbf{A}$. Taking into account these facts, if Eq. (B.1) is transposed and differentiated with respect to time, the following relation is found:

$$\dot{\mathbf{B}} \, \mathbf{\Phi}(\mathbf{u})^{\mathrm{T}} = \dot{\mathbf{\Phi}}(\mathbf{Au})^{\mathrm{T}} \mathbf{A} + \mathbf{\Phi}(\mathbf{Au})^{\mathrm{T}} \dot{\mathbf{A}}. \tag{B.2}$$

Eqs. (B.1) and (B.2) can be multiplied to obtain

$$\dot{\mathbf{B}} \, \mathbf{\Phi}(\mathbf{u})^{\mathrm{T}} \mathbf{\Phi}(\mathbf{u}) \mathbf{B}^{\mathrm{T}} = \dot{\mathbf{\Phi}}(\mathbf{Au})^{\mathrm{T}} \mathbf{A} \mathbf{A}^{\mathrm{T}} \mathbf{\Phi}(\mathbf{Au}) + \mathbf{\Phi}(\mathbf{Au})^{\mathrm{T}} \dot{\mathbf{A}} \, \mathbf{A}^{\mathrm{T}} \mathbf{\Phi}(\mathbf{Au}). \tag{B.3}$$

Now an integration is carried out over the RC volume, giving

$$\dot{\mathbf{B}} \int_{\mathrm{RCV}} \rho \boldsymbol{\Phi}(\mathbf{u})^{\mathrm{T}} \boldsymbol{\Phi}(\mathbf{u}) \, \mathrm{d}\upsilon \, \mathbf{B}^{\mathrm{T}} = \int_{\mathrm{RCV}} \rho \left(\dot{\boldsymbol{\Phi}}(\mathbf{Au})^{\mathrm{T}} \boldsymbol{\Phi}(\mathbf{Au}) + \boldsymbol{\Phi}(\mathbf{Au})^{\mathrm{T}} \Omega \mathbf{J} \boldsymbol{\Phi}(\mathbf{Au}) \right) \mathrm{d}\upsilon. \tag{B.4}$$

Further operations lead to

$$\mathbf{Z}\Omega = \dot{\mathbf{B}} \, \mathbf{B}^{\mathrm{T}} = \int_{\mathrm{RCV}} \rho \left(\dot{\boldsymbol{\Phi}}(\mathbf{v})^{\mathrm{T}} \boldsymbol{\Phi}(\mathbf{v}) + \Omega \boldsymbol{\Phi}(\mathbf{v})^{\mathrm{T}} \mathbf{J} \boldsymbol{\Phi}(\mathbf{v}) \right) \mathrm{d}\upsilon. \tag{B.5}$$

From the expression

$$\dot{\boldsymbol{\Phi}}(\mathbf{v}) = \sum_{i=1}^{3} \frac{\partial \boldsymbol{\Phi}(\mathbf{v})}{\partial v_i} \dot{v}_i = \sum_{i=1}^{3} \frac{\partial \boldsymbol{\Phi}(\mathbf{v})}{\partial v_i} \left(\frac{\mathrm{d}\mathbf{v}}{\mathrm{d}t} \right)_i = \sum_{i=1}^{3} \frac{\partial \boldsymbol{\Phi}(\mathbf{v})}{\partial v_i} (\dot{\mathbf{A}} \, \mathbf{u})_i = \sum_{i=1}^{3} \frac{\partial \boldsymbol{\Phi}(\mathbf{v})}{\partial v_i} (\dot{\mathbf{A}} \, \mathbf{A}^{\mathrm{T}} \mathbf{v})_i = \Omega \sum_{i=1}^{3} \frac{\partial \boldsymbol{\Phi}(\mathbf{v})}{\partial v_i} (\mathbf{Jv})_i, \tag{B.6}$$

Eq. (26) is found.

Appendix C

Demonstration of Eq. (20)

$$\begin{aligned} \mathbf{B}\tilde{\mathbf{J}}\mathbf{B}^{\mathrm{T}} &= \mathbf{B} \int_{\mathrm{RCV}} \rho \boldsymbol{\Phi}(\mathbf{u})^{\mathrm{T}} \mathbf{J} \boldsymbol{\Phi}(\mathbf{u}) \, \mathrm{d}\upsilon \mathbf{B}^{\mathrm{T}} = \int_{\mathrm{RCV}} \rho \mathbf{B} \boldsymbol{\Phi}(\mathbf{u})^{\mathrm{T}} \mathbf{A}_{\theta} \mathbf{A}^{\mathrm{T}} \boldsymbol{\Phi}(\mathbf{u}) \mathbf{B}^{\mathrm{T}} \, \mathrm{d}\upsilon \\ &= \int_{\mathrm{RCV}} \rho \boldsymbol{\Phi}(\mathbf{Au})^{\mathrm{T}} \mathbf{A} \mathbf{A}_{\theta} \mathbf{A}^{\mathrm{T}} \mathbf{A}^{\mathrm{T}} \boldsymbol{\Phi}(\mathbf{Au}) \, \mathrm{d}\upsilon = \int_{\mathrm{RCV}} \rho \boldsymbol{\Phi}(\mathbf{Au})^{\mathrm{T}} \mathbf{A} \mathbf{A}^{\mathrm{T}} \mathbf{A}_{\theta} \mathbf{A}^{\mathrm{T}} \boldsymbol{\Phi}(\mathbf{Au}) \, \mathrm{d}\upsilon \\ &= \int_{\mathrm{RCV}} \rho \boldsymbol{\Phi}(\mathbf{Au})^{\mathrm{T}} \mathbf{J} \boldsymbol{\Phi}(\mathbf{Au}) \, \mathrm{d}\upsilon = \int_{\mathrm{RCV}} \rho \boldsymbol{\Phi}(\mathbf{v})^{\mathrm{T}} \mathbf{J} \boldsymbol{\Phi}(\mathbf{v}) \, \mathrm{d}\upsilon = \tilde{\mathbf{J}}. \end{aligned} \tag{C.1}$$

Demonstration of Eq. (22)

$$\begin{aligned} \mathbf{B}\tilde{\mathbf{E}}\mathbf{B}^{\mathrm{T}} &= \mathbf{B} \int_{\mathrm{RCV}} \rho \boldsymbol{\Phi}(\mathbf{u})^{\mathrm{T}} \mathbf{E} \boldsymbol{\Phi}(\mathbf{u}) \, \mathrm{d}\upsilon \mathbf{B}^{\mathrm{T}} = - \int_{\mathrm{RCV}} \rho \mathbf{B} \boldsymbol{\Phi}(\mathbf{u})^{\mathrm{T}} \mathbf{A}_{\theta\theta} \mathbf{A}^{\mathrm{T}} \boldsymbol{\Phi}(\mathbf{u}) \mathbf{B}^{\mathrm{T}} \, \mathrm{d}\upsilon \\ &= - \int_{\mathrm{RCV}} \rho \boldsymbol{\Phi}(\mathbf{Au})^{\mathrm{T}} \mathbf{A} \mathbf{A}_{\theta\theta} \mathbf{A}^{\mathrm{T}} \mathbf{A}^{\mathrm{T}} \boldsymbol{\Phi}(\mathbf{Au}) \, \mathrm{d}\upsilon = - \int_{\mathrm{RCV}} \rho \boldsymbol{\Phi}(\mathbf{Au})^{\mathrm{T}} \mathbf{A} \mathbf{A}^{\mathrm{T}} \mathbf{A}_{\theta\theta} \mathbf{A}^{\mathrm{T}} \boldsymbol{\Phi}(\mathbf{Au}) \, \mathrm{d}\upsilon \\ &= \int_{\mathrm{RCV}} \rho \boldsymbol{\Phi}(\mathbf{Au})^{\mathrm{T}} \mathbf{E} \boldsymbol{\Phi}(\mathbf{Au}) \, \mathrm{d}\upsilon = \int_{\mathrm{RCV}} \rho \boldsymbol{\Phi}(\mathbf{v})^{\mathrm{T}} \mathbf{E} \boldsymbol{\Phi}(\mathbf{v}) \, \mathrm{d}\upsilon = \tilde{\mathbf{E}}. \end{aligned} \tag{C.2}$$

Demonstration of Eq. (23)

$$\begin{aligned} \mathbf{B}\tilde{\mathbf{J}}\dot{\mathbf{B}}^{\mathrm{T}} &= \mathbf{B} \int_{\mathrm{RCV}} \rho \boldsymbol{\Phi}(\mathbf{u})^{\mathrm{T}} \mathbf{J} \boldsymbol{\Phi}(\mathbf{u}) \, \mathrm{d}\upsilon \dot{\mathbf{B}}^{\mathrm{T}} = \int_{\mathrm{RCV}} \rho \mathbf{B} \boldsymbol{\Phi}(\mathbf{u})^{\mathrm{T}} \mathbf{A}_{\theta} \mathbf{A}^{\mathrm{T}} \boldsymbol{\Phi}(\mathbf{u}) \mathbf{B}^{\mathrm{T}} \mathbf{B} \dot{\mathbf{B}}^{\mathrm{T}} \, \mathrm{d}\upsilon \\ &= \Omega \int_{\mathrm{RCV}} \rho \boldsymbol{\Phi}(\mathbf{Au})^{\mathrm{T}} \mathbf{A} \mathbf{A}_{\theta} \mathbf{A}^{\mathrm{T}} \mathbf{A}^{\mathrm{T}} \boldsymbol{\Phi}(\mathbf{Au}) \mathbf{Z}^{\mathrm{T}} \, \mathrm{d}\upsilon = \Omega \int_{\mathrm{RCV}} \rho \boldsymbol{\Phi}(\mathbf{Au})^{\mathrm{T}} \mathbf{A} \mathbf{A}^{\mathrm{T}} \mathbf{A}_{\theta} \mathbf{A}^{\mathrm{T}} \boldsymbol{\Phi}(\mathbf{Au}) \mathbf{Z}^{\mathrm{T}} \, \mathrm{d}\upsilon \\ &= \Omega \int_{\mathrm{RCV}} \rho \boldsymbol{\Phi}(\mathbf{Au})^{\mathrm{T}} \mathbf{J} \boldsymbol{\Phi}(\mathbf{Au}) \, \mathrm{d}\upsilon \mathbf{Z}^{\mathrm{T}} = \Omega \int_{\mathrm{RCV}} \rho \boldsymbol{\Phi}(\mathbf{u})^{\mathrm{T}} \mathbf{J} \boldsymbol{\Phi}(\mathbf{u}) \, \mathrm{d}\upsilon \mathbf{Z}^{\mathrm{T}} = 2\Omega^2 \tilde{\mathbf{J}} \, \mathbf{Z}^{\mathrm{T}}. \end{aligned} \tag{C.3}$$

The demonstration of Eq. (21) is due to the fact that the set $\mathbf{q}$ consists of modal coordinates, and consequently the elastic energy is

$$V = \frac{1}{2} \left(\mathbf{q}^{\mathrm{T}} \tilde{\mathbf{K}} \, \mathbf{q} \right). \tag{C.4}$$

The non-zero terms in $\mathbf{L}$ are associated with modes with multiplicity 1. The rows and columns of $\mathbf{B}$ related to modes with multiplicity 1 are 0 (off-diagonal) or 1 (diagonal). Consequently, Eq. (24) is fulfilled.

References

[1] S.H. Choi, C. Pierre, A.G. Ulsoy, Consistent modeling of rotating Timoshenko shafts subject to axial loads, *Journal of Vibration and Acoustics-Transactions of the ASME* 114 (1992) 249–259.
[2] M.A. Hili, T. Fakhfakh, M. Haddar, Vibration analysis of a rotating flexible shaft–disk system, *Journal of Engineering Mathematics* 57 (2007) 351–363.
[3] S.C. Hsieh, J.H. Chen, A.C. Lee, A modified transfer matrix method for the coupling lateral and torsional vibrations of symmetric rotor-bearing systems, *Journal of Sound and Vibration* 289 (2006) 294–333.
[4] S.K. Sinha, Dynamic characteristics of a flexible bladed-rotor with Coulomb damping due to tip-rub, *Journal of Sound and Vibration* 273 (2004) 875–919.
[5] C.W. Tseng, J.Y. Shen, I.Y. Shen, Vibration of rotating-shaft HDD spindle motors with flexible-stationary parts, *IEEE Transactions on Magnetics* 39 (2003) 794–799.
[6] H.A. Hussien, A.A. Shabana, W.J. Tsung, M.R. Fetcho, Dynamic and vibration analysis of a vehicle rear axle system, *Vehicle System Dynamics* 33 (2000) 205–231.
[7] H. Ouyang, J.E. Mottershead, Vibration of a beam excited by a moving flexible body, *Applied Mechanics and Materials*, v 5-6, *Modern Practice in Stress and Vibration Analysis VI—Proceedings of the Sixth International Conference on Modern Practice in Stress and Vibration Analysis*, 2006, pp. 457–464.
[8] G.J. Sheu, S.M. Yang, Dynamic analysis of a spinning Rayleigh beam, *International Journal of Mechanical Sciences* 47 (2005) 157–169.
[9] J. Fayos, A. Rovira, L. Baeza, J. Carballeira, Rotating shaft analytical response in adimensional form, *Proceedings of the 13th International Congress on Sound and Vibration*, Vienna, 2006.
[10] M.A. Brown, A.A. Shabana, Application of multibody methodology to rotating shaft problems, *Journal of Sound and Vibration* 204 (1997) 439–457.
[11] A.A. Shabana, *Dynamics of Multibody Systems*, Wiley, New York, 1989.
[12] G.T. Mase, G.E. Mase, *Continuum Mechanics for Engineers*, CRC Press, Boca Raton, FL, 1999.
[13] ⟨http://www.ce.berkeley.edu/~rlt/feap/⟩
[14] W. Weaver Jr., S.P. Timoshenko, D.H. Young, *Vibration Problems in Engineering*, Wiley, New York, 1990.